Selection of cathode contact materials for solid oxide fuel cells

Michael C. Tucker*, Lei Cheng, Lutgard C. DeJonghe

Materials Sciences Division, Lawrence Berkeley National Laboratory, 1 Cyclotron Rd, Berkeley, CA 94720, United States

ABSTRACT

The goal of this work is to identify suitable cathode contact materials (CCM) to bond and electrically connect LSCF cathode to $Mn_{1.5}Co_{1.5}O_4$-coated 441 stainless steel after sintering at the relatively low temperature of 900–1000 °C. A wide variety of CCM candidates are synthesized and characterized. For each, the conductivity, coefficient of thermal expansion, sintering behavior, and tendency to react with LSCF or $Mn_{1.5}Co_{1.5}O_4$ are determined. From this screening, LSCF, LSCuF, LSC, and SSC are selected as the most promising candidates. These compositions are applied to LSCF and $Mn_{1.5}Co_{1.5}O_4$-coated 441 stainless steel coupons and subjected to 200 h ASR testing at 800 °C. After area-specific resistance testing, the specimens are cross-sectioned and analyzed for interdiffusion across the CCM/LSCF or CCM/$Mn_{1.5}Co_{1.5}O_4$ interfaces. A relatively narrow band of interdiffusion is observed.

1. Introduction

Assembly of solid oxide fuel cell (SOFC) stacks typically involves mechanically and electrically connecting a number of cells and interconnects in series. Connection of the cathode to the interconnect (or coating on the interconnect) is usually accomplished by compression of the stack using an external load frame, and is often aided by the use of a cathode contact material (CCM). The CCM is an electrically conductive material, and is applied as a paste or ink during stack assembly to form a continuous layer or discrete contact pads. The CCM provides electrical connection between the cathode and interconnect, and can also serve to improve in-plane conduction over the area of the cathode. Fig. 1 indicates placement of the CCM in the fuel cell stack.

Often, the CCM is simply a thick layer of the electrocatalyst used in the cathode. For example, a thin LSM-YSZ cathode layer optimized for electrochemical activity can be covered with a thick LSM CCM layer optimized for gas transport and electrical conductivity. Recent studies of CCM behavior utilized some of the known SOFC cathode materials, such as: LSM, LSC, LSCM, and LSF [1]; LSCMF, LSF, LSCM, LNF, LSCF, and LSCCu [2]. These materials typically require firing at high temperature (>1100 °C) to achieve good sintering and effective bonding within the CCM layer and at the CCM/interconnect and CCM/cathode interfaces. Efforts to decrease the required sintering temperature through doping [3] and control of the defect structure [3,4] have had some success.

The state-of-the-art preferred interconnect material is ferritic stainless steel, primarily chosen for low cost and ease of fabrication.

To avoid excessive oxidation of the stainless steel interconnect, heating steps during assembly of the stack must be limited to below 1000 °C and operation of the fuel cell occurs at no more than 850 °C [5,6]. This means that, in practice, significant sintering of the CCM material is difficult to achieve when using stainless steel interconnects. Therefore, the CCM layer is often a loosely packed bed of conductive particles. This is acceptable if there is suitable external compression to create good mechanical contact between the cathode, CCM, and interconnect. However, uniform compressive loads across the entire area of the cell or stack are rarely achieved in practice. Thermal gradients across the cell area, and thermal transients during stack heat-up and cool-down can cause warping of the cells and interconnects, leading to delamination of the CCM from the cathode or interconnect. Such delamination is accompanied by significant loss of electrical contact between the cell and interconnect. Therefore, it is desirable to choose a CCM composition that will sinter during stack heat-up to create a strong, conductive layer that is well-bonded to the interconnect and cathode. The fundamental challenge in CCM selection is to identify a material which is reactive enough to bond or sinter at 1000 °C or lower, but stable enough for long-term operation at 750–850 °C.

2. Approach

The CCM composition must fulfill the following requirements:

- high electronic conductivity;
- sintering/bonding at 900–1000 °C;
- good coefficient of thermal expansion (CTE) match to other cell components;

---

* Corresponding author. Tel.: +1 510 486 5304; fax: +1 510 486 4881.
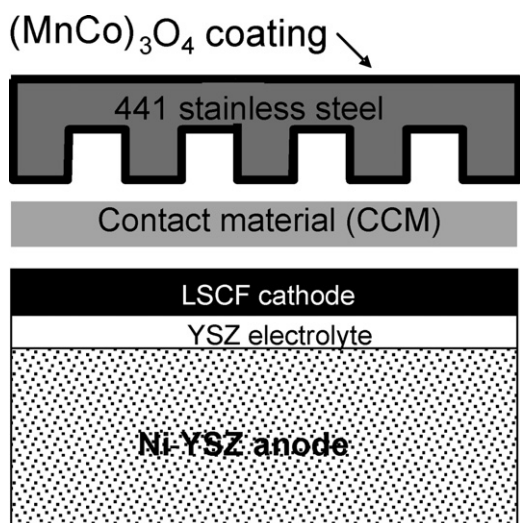E-mail address: mctucker@lbl.gov (M.C. Tucker).

Fig. 1. Schematic representation of CCM placed between SOFC cell and coated stainless steel interconnect.

- does not react deleteriously with the chosen neighbor materials, LSCF cathode and $(Mn,Co)_3O_4$ coating for the stainless steel interconnect [6,7].

Unlike cathode catalysts, the CCM does not need to display ionic conductivity or electrochemical activity. Even so, we chose known SOFC cathode materials as the first candidates for application as CCM compositions because they are likely to fulfill the above requirements. The cathode literature was reviewed for promising candidate compositions [8–19]. Table 1 lists the selected compositions and their abbreviations. Reporting of the relevant properties, such as conductivity and sintering behavior, is not complete for many of these materials. Furthermore, materials that are well-characterized have often been synthesized and analyzed by various methods, complicating comparison. For example, the conductivity of LNF varies significantly with synthesis method and final sintering temperature [21].

Our approach is therefore to synthesize the list of candidate compositions and use standard protocols to assess the required properties listed above. The result of this screening effort is a short list of most promising candidates which are then applied to stainless steel interconnects and LSCF coupons for long-term area specific resistance (ASR) testing.

Table 1
List of selected compositions and their abbreviations.

$La_{0.6}Sr_{0.4}Co_{0.8}Fe_{0.2}O_3$	LSCF
$La_{0.8}Sr_{0.2}Cu_{0.9}Fe_{0.1}O_{2.5}$	LSCuF
$La_{0.7}Sr_{0.3}CoO_3$	LSC
$Sm_{0.5}Sr_{0.5}CoO_3$	SSC
$SmBa_{0.5}Sr_{0.5}Co_2O_5$	SBSC
$GdSrCo_2O_5$	GSC
$La_{0.65}Sr_{0.3}MnO_3$	LSM
$LaBaCo_2O_5$	LBC
$YBaCo_2O_5$	YBC
$Nd_{1.8}Ce_{0.2}CuO_4$	NCC
$La_{0.8}Sr_{0.2}Co_{0.3}Mn_{0.1}Fe_{0.6}O_3$	LSCMF
$La_{0.98}Ni_{0.6}Fe_{0.4}O_3$	LNF
$La_{1.2}Sr_{0.8}NiO_4$	LSN
$La_{0.7}Sr_{0.3}FeO_3$	LSF
$La_2Ni_{0.6}Cu_{0.4}O_4$	LNC

Table 2
Sintering temperature used for fabrication of bar specimens for conductivity measurements.

Composition	Sintering temperature (°C)
LSM	1300
LSCF	1300
LSC	1300
LSCMF	1300
LNF	1300
LSN	1300
LSF	1300
LNC	1300
SSC	1200
SBSC	1200
LBC	1200
GSC	1100
YBC	1100
NCC	1100
LSCuF	1000

3. Experimental methods

3.1. Synthesis and phase characterization

Powders of SSC, LNF, LSCF, and LSM were purchased from Praxair. All others were synthesized by glycine nitrate combustion process (GNP), followed by calcining at 800 °C in air for 4 h. X-ray diffraction (XRD) (Philips X'Pert) was used to check for the correct phase. If it was not found, the powder was calcined at increasing temperature (100 °C increments) until the intended phase was formed, with no significant secondary phases present.

3.2. Conductivity

Calcined powder of each composition was ball-milled with binder (PVB, DBT, MFO) in IPA, dried, sieved, and pressed into bars. The bars were sintered at various temperatures shown in Table 2 to achieve full density. The dimensions of the sintered bars were about 1.5 mm × 3 mm × 40 mm. Pt mesh current leads were applied to the ends of the bars with Pt paste, and Pt wire voltage leads were wrapped around the bar at 0.5 cm to either side of the centerline. Four-probe DC resistance measurements were taken at 650–900 °C in air using a potentiostat-galvanostat (Biologic VMP-3).

3.3. CTE

Small pellets of powder and binder were sintered to the temperatures in Table 2 (as above). The sintered pellets were then loaded into a contacting dilatometer (Linseis L75) for CTE measurement from 300 to 900 °C in air with a heating rate of 3 °C min^{-1}.

3.4. Dilatometry

Small pellets of powder and binder (as above) were sintered in a contacting dilatometer (Linseis L75) in air from room temperature to 1100–1300 °C (depending on powder melting temperature). The heating rate was 3 °C min^{-1}, followed by a 2 h hold at the maximum temperature. The data presented below in Section 4.5 have been adjusted to remove binder burnout, such that the zero-point occurs at 600 °C (above binder features, and below sintering features).

3.5. Reaction mixtures

To determine extent of reaction between the CCM and MCO $(Mn_{1.5}Co_{1.5}O_4)$ or LSCF, pellets of CCM–MCO and CCM–LSCF mixed powder (50:50 wt) were prepared and coarsened in air at 1000 °C for 10 h or 800 °C for 120 h. The pellets were then analyzed by XRD
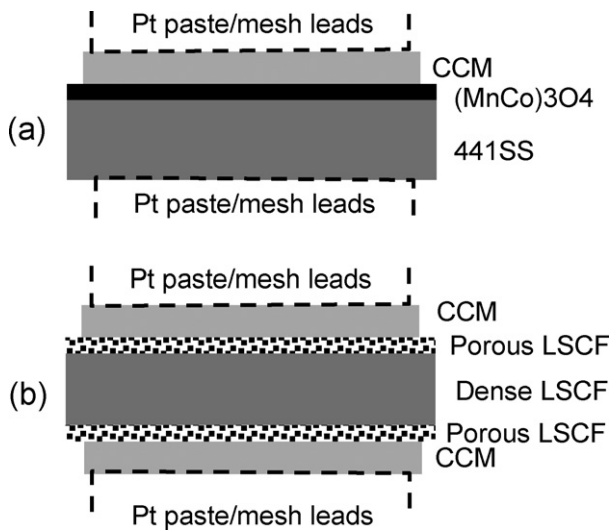
Fig. 2. Schematic representation of "half-assembly" specimen geometries. (a) CCM/MCO-441 and (b) CCM/LSCF.

and SEM/EDAX (Hitachi S4300SE/N) to determine extent of reaction and interdiffusion between the materials.

3.6. ASR measurements

Specimens for area-specific resistance (ASR) measurements were prepared according to the geometries in Fig. 2. Various CCM inks were prepared by mixing the powder with Ferro B75717 printing vehicle. 441 stainless steel coupons were coated with MCO by screenprinting at Pacific Northwest National Laboratory (PNNL). LSCF coupons were prepared by ball-milling LSCF powder with binder (PVB, DBT, MFO) in IPA. The powder was then dried, sieved, and pressed into coupons and sintered at 1200 °C for 2 h. LSCF ink was screenprinted onto both sides of the coupon and sintered at 1050 °C for 2 h to produce a porous LSCF layer coating the dense LSCF coupon. CCM layers were then screenprinted onto the MCO or porous LSCF layer, dried under a heatlamp and sintered in air at 1000 °C for 1.5 (NCC, LSC, LSCuF) or 2 h (LSCF, SSC). Pt paste (Heraeus CL11–5349) and Pt mesh (Alfa Aesar 10283) were applied as current collectors on the CCM layers, and sintered at 800 °C. Pt mesh was spot-welded to the 441 coupon. LSCF/CCM/MCO-441 specimens were prepared according to the geometry in Fig. 2a, with an additional LSCF layer printed on the CCM before application of the Pt paste. The ASR specimens were then subjected to 500 mA current for 200 h at 800 °C in air. DC current was applied in a 4-probe configuration using a Biologic VMP3 potentiostat. ASR values for CCM/LSCF were divided by 2 to obtain the per-interface ASR reported in Section 4.7.

3.7. Post-test analysis

After ASR testing, the specimens were mounted in epoxy, cross-sectioned, polished, and analyzed with SEM and EDS (Hitachi S4300SE/N).

4. Results and discussion

4.1. Powder phase characterization

X-ray diffraction (XRD) was used to check the phase of the candidate powders. XRD traces are shown in Figs. 3–5. Small peaks arising from the XRD specimen holder are observable at 42°, 44°, 49°, 51°, and 73°. Fig. 3 shows XRD traces for the powders pur-
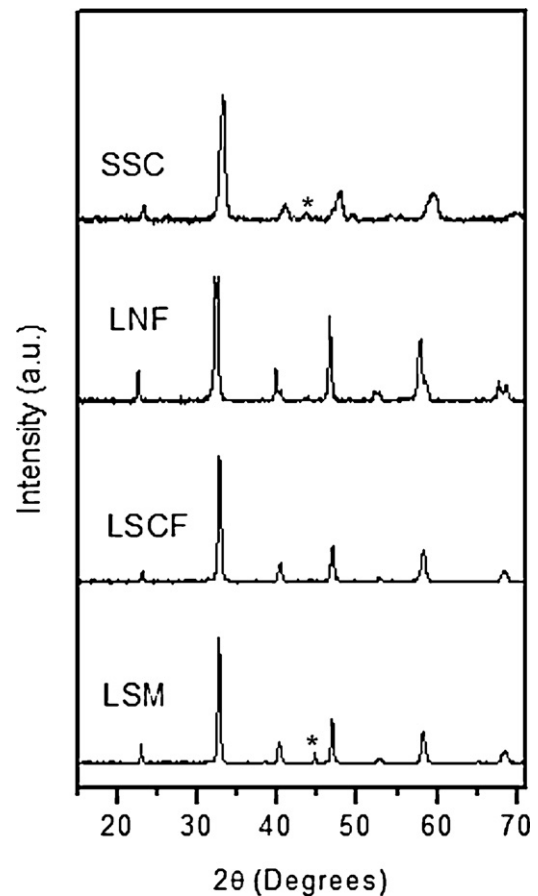

Fig. 3. XRD traces of powders purchased from Praxair. Peaks arising from the sample holder are indicated with an asterisk.
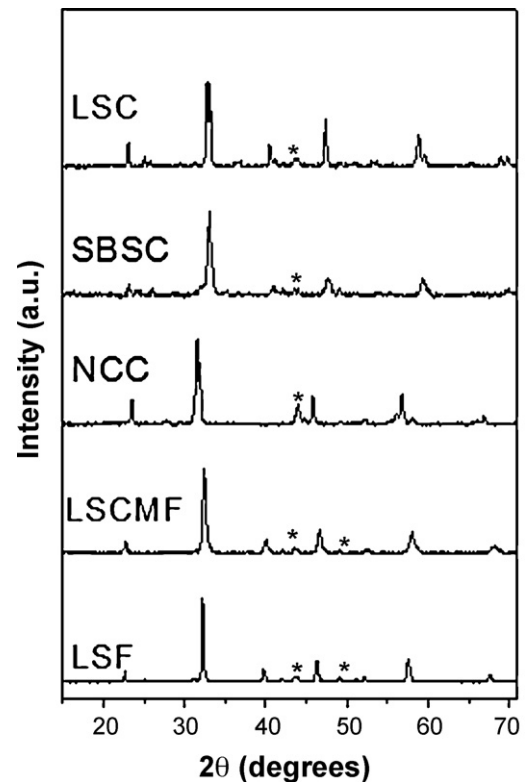

Fig. 4. XRD traces of powders synthesized by GNP and coarsened at 800 °C. Peaks arising from the sample holder are indicated with an asterisk.
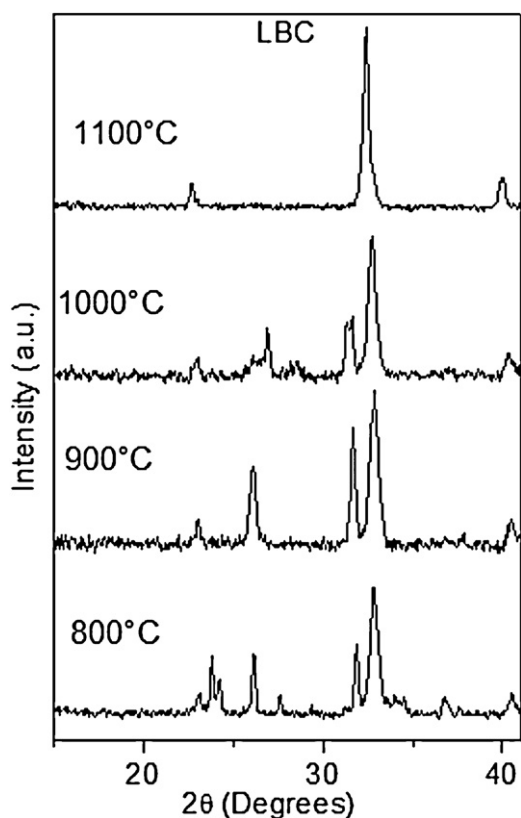
Fig. 5. XRD traces of LBC synthesized by GNP and coarsened to various temperatures.

chased from Praxair. All display the expected perovskite phase. Fig. 4 shows several candidate compositions that crystallized in the intended phase after calcining at 800 °C. All other candidate compositions required calcination at higher temperatures to produce the intended pure phase. For example, LBC required calcination to 1100 °C as shown in Fig. 5. GSC and LSN required 900 °C, LSCuF required 1000 °C, and YBC required 1200 °C (not shown). In all cases, the XRD traces for the intended phases are consistent with previous literature reports [9–19].

4.2. Conductivity

Conductivity of the CCM is one of the most important properties for assuring acceptable ASR. Conductivity is expected to be a strong function of microstructure and therefore sintering temperature, as it is dependent on porosity and inter-particle neck formation [22]. The two obvious choices for microstructure for the conductivity measurement specimens are: (a) full density, or (b) the microstructure achieved after sintering at 1000 °C, which is relevant to the conditions during cell-to-interconnect bonding. We chose to measure the conductivity at full density, as this provides the fundamental material property. This provides a "best-case" conductivity and allows ranking of the various compositions. Also, future work will focus on optimizing the microstructure achieved after sintering at 1000 °C by use of sintering aids, particle size distribution optimization, mixtures of compositions, and other methods. The conductivity after sintering the present powders at 1000 °C may not be relevant to what can be achieved after optimization, but the bulk material conductivity provides a useful upper boundary to the conductivity.

Bars of each candidate material were sintered to full density and assessed for total conductivity over the range 650–900 °C, using 4-probe DC analysis. The results are shown in Fig. 6. In all cases, conductivity was a weak function of temperature, consistent
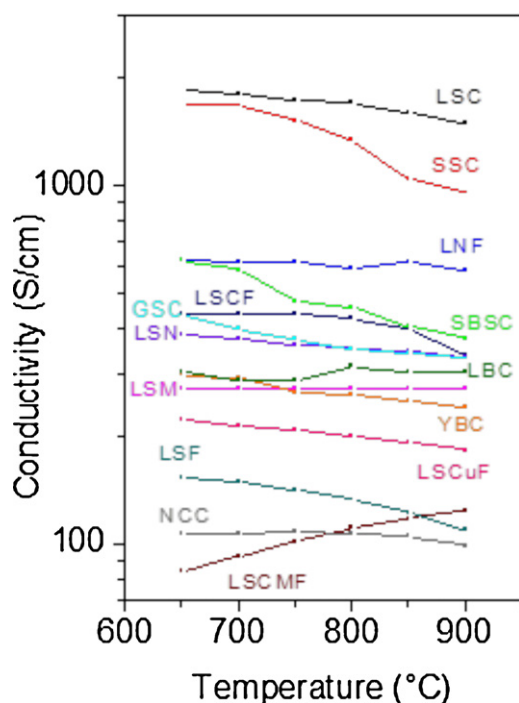

Fig. 6. Temperature-dependence of the conductivity of various specimen bars sintered at the temperatures listed in Table 2.

with previous reports [7,16,20,23]. The measured conductivities spanned more than an order of magnitude, with LSC and SSC displaying conductivity greater than 1000 S cm^{-1}, as reported previously [20,23]. Note that the conductivity obtained for LNCu was about 10 S cm^{-1} and is therefore not shown in Fig. 6. The conductivity at 800 °C for each candidate is listed in Table 3.

4.3. CTE

Coefficient of thermal expansion (CTE) was measured for dense pellets of each candidate composition. The results are compiled in Fig. 7, and the CTE at 800 °C is listed in Table 3. The CTE reported is calculated relative to room temperature. A wide range of CTE is observed; the CTE for LBC is about twice that for 441 steel and other common SOFC materials. Although such disparate values of CTE present an obvious concern for integrity of the CCM layer and interfaces during thermal cycling, we have chosen to not eliminate any candidates from consideration solely on the basis of displaying a large CTE. The CCM layer will be relatively thin, porous, and bounded on both sides by the cell and interconnect which have relatively well-matched CTE, all of which are expected to reduce thermal stress. All of these materials have been successfully employed as cathodes, despite having CTE larger than YSZ [9–19].

4.4. Reaction of CCM with MCO and LSCF

It is desirable that the CCM composition does not react significantly with the cathode material (LSCF) or the steel coating material (MCO). A minimal amount of reaction is acceptable if the following conditions are satisfied:

- reaction products are stable and display high conductivity;
- reaction improves or does not decrease bonding;
- reaction is limited to the CCM/LSCF interface, so that cathode operation at the cathode/electrolyte interface is not compromised.

Table 3

Summary of screening results for various CCM candidates. Colors indicate the relative merit of each property (green, yellow, orange and red indicate best, good, marginal, and poor, respectively).

	Incipient Sintering Point (°C)	Shrinkage at 900°C (%)	Shrinkage at 1000°C (%)	CTE at 800°C (ppm/K)	Reacts with MCO? 800°C 120h	Reacts with MCO? 1000°C 10h	Reacts with LSCF? 800°C 120h	Reacts with LSCF? 1000°C 10h	Conductivity of bulk dense pellet at 800°C (S/cm)
LSCF	637	2.7	7.6	17.3	NO	NO	N/A	N/A	426
LSCuF	820	1.1	10.1	15.5	NO	NO	NO	NO	201
LSC	677	1.1	3.3	18.7	NO	NO	Minor	Minor	1702
SSC	740	0.5	2.3	22	NO	Trace	NO	NO	1338
SBSC	708	1.6	3.4	22	NO	Trace	YES	YES	458
GSC	760	1.3	3.2	19.5	NO	Trace	YES	YES	350
LSM	784	0.7	3.3	12.8	NO	NO	YES	YES	272
LBC	770	0.7	2.3	25	NO	NO	Minor	Minor	314
YBC	689	1.7	3.8	16.8	NO	YES	YES	YES	260
NCC	657	1.5	5.5	14.5	YES	YES	YES	YES	107
LSCMF	786	0.4	2.1	17.6	NO	NO	N/A	N/A	110
LNF	932	0	1.1	13.8	NO	NO	YES	YES	589
LSN	975	0	0.1	13.5	Minor	YES	NO	NO	352
LSF	690	0.3	0.9	13.3	NO	NO	NO	NO	133
LNC	782	0.4	2.4	14.6	NO	NO	NO	NO	11

The reactivity of various CCM compositions with LSCF or MCO was determined by mixing 10–75 μm powder agglomerates of the materials together, pressing into a pellet, and calcining at two temperatures:

- 800 °C for 120 h to mimic SOFC operation conditions;
- 1000 °C for 10 h to mimic worst-case CCM bonding conditions.

XRD was used to ascertain extent-of-reaction after calcination. Selected XRD data is shown below. All results are reported in Table 3.
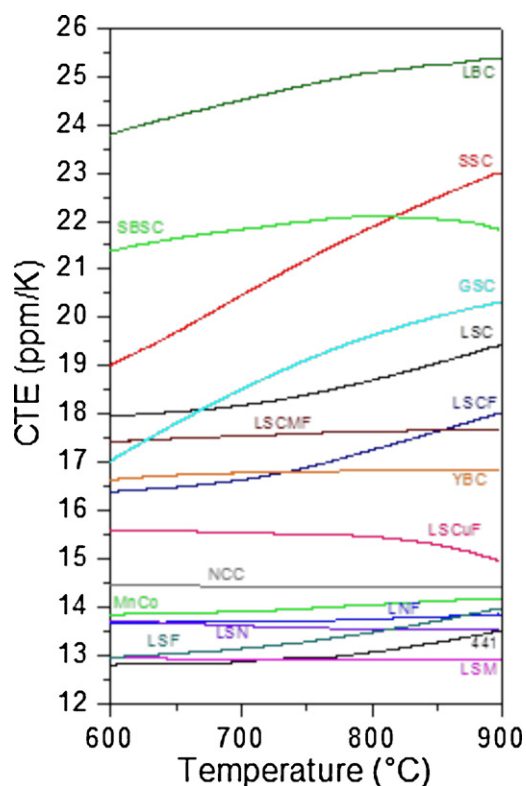

Fig. 7. Temperature-dependence of the coefficient of thermal expansion (CTE) of various CCM candidates.

A classic example of a mixture exhibiting no reaction is shown in Fig. 8a. In this case, a mixture of LSCF and MCO was calcined at 1000 °C for 10 h. The XRD trace for the mixed and calcined composition (black) is a simple superposition of the traces for the two pure powders (red and magenta). No new peaks arise after calcining, nor are any peaks missing. The relative heights and shapes of all the peaks for each component are the same for the pure component and in the mixture. For the case of NCC and MCO, significant reaction is observed after 800 °C calcination as shown in Fig. 8b. Peaks arising from pure NCC dominate the XRD trace, but several new peaks are present, suggesting formation of a reaction product. All of the peaks arising from MCO disappear after calcination, suggesting MCO is consumed by reaction. Similar changes are observed for the LSCF and SBSC mixture calcined at 1000 °C for 10 h, again suggesting significant reaction as shown in Fig. 8c. Similar analysis was applied to all other mixtures studied, and the results are reported in Table 3. Those entries labeled as "minor" reaction showed a noticeably lesser degree of consumption of the original phases or appearance of new phases compared to the results shown in Fig. 8b and c. Note that a conclusion could not be drawn for LSCMF/LSCF. Because of their similar composition and structure, the XRD peaks of these candidates overlapped. Therefore, we were not able to observe evidence of reaction, nor could we rule it out. We presume some interdiffusion between LSCMF and LSCF does occur.

SEM/EDAX was used to analyze the extent of interdiffusion for mixtures that reacted during calcination. Results for LSCF and NCC calcined at 1000 °C for 10 h are shown in Fig. 9. The position of the interface between LSCF and NCC regions was estimated visually by the porosity and color contrast visible in Fig. 9. We assume that this is the original interface, and growth of either phase did not occur. A line scan across the interface between the two compositions reveals that minimal interdiffusion of La, Sr, Fe, Co, Cu or Ce occurred. Nd, however, diffused significantly into LSCF. The radius of the LSCF particles in the sample was roughly 20 μm. Extrapolating the Nd concentration curve suggests that interdiffusion would be limited to roughly the 40 μm of LSCF near the LSCF/NCC interface for larger particles. This leads us to predict that, although LSCF and NCC interact, the buried electrochemical interface in a LSCF layer thicker than about 40 μm would not be affected by short processing steps at 1000 °C. In fact, it is possible that this interdiffusion may be useful to promote bonding at the LSCF/NCC interface. Similar
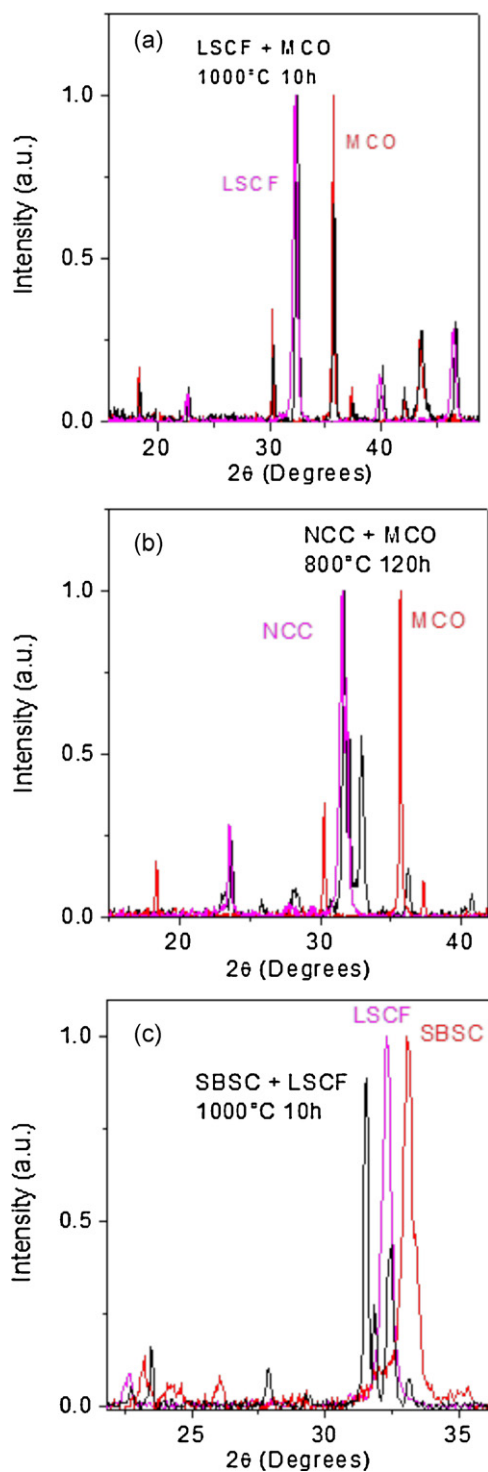
Fig. 8. XRD traces of various physical mixtures after exposure to high temperature. XRD traces of the pure components of each mixture are shown for comparison. (a) LSCF and MCO mixture after exposure to 1000 °C for 10 h; (b) NCC and MCO mixture after exposure to 800 °C for 120 h; and (c) SBSC and LSCF mixture after exposure to 1000 °C for 120 h.

Fig. 9. SEM and EDS analyses of physical mixtures of NCC with LSCF or MCO after exposure to 1000 °C for 10 h. (a) SEM image of LSCF and NCC mixture. The arrow indicates the location of EDS analysis points. (b) EDS signal intensity for various elements in the NCC and LSCF mixture. (c) EDS signal intensity for various elements in the NCC and MCO mixture. The dashed lines indicate the position of the LSCF/NCC or MCO/NCC boundary.

analysis for MCO and NCC calcined at 1000 °C for 10 h are shown in Fig. 9c. In this case, diffusion of the NCC components into MCO is not observed, but Mn and Co diffuse about 30 μm into the NCC region.
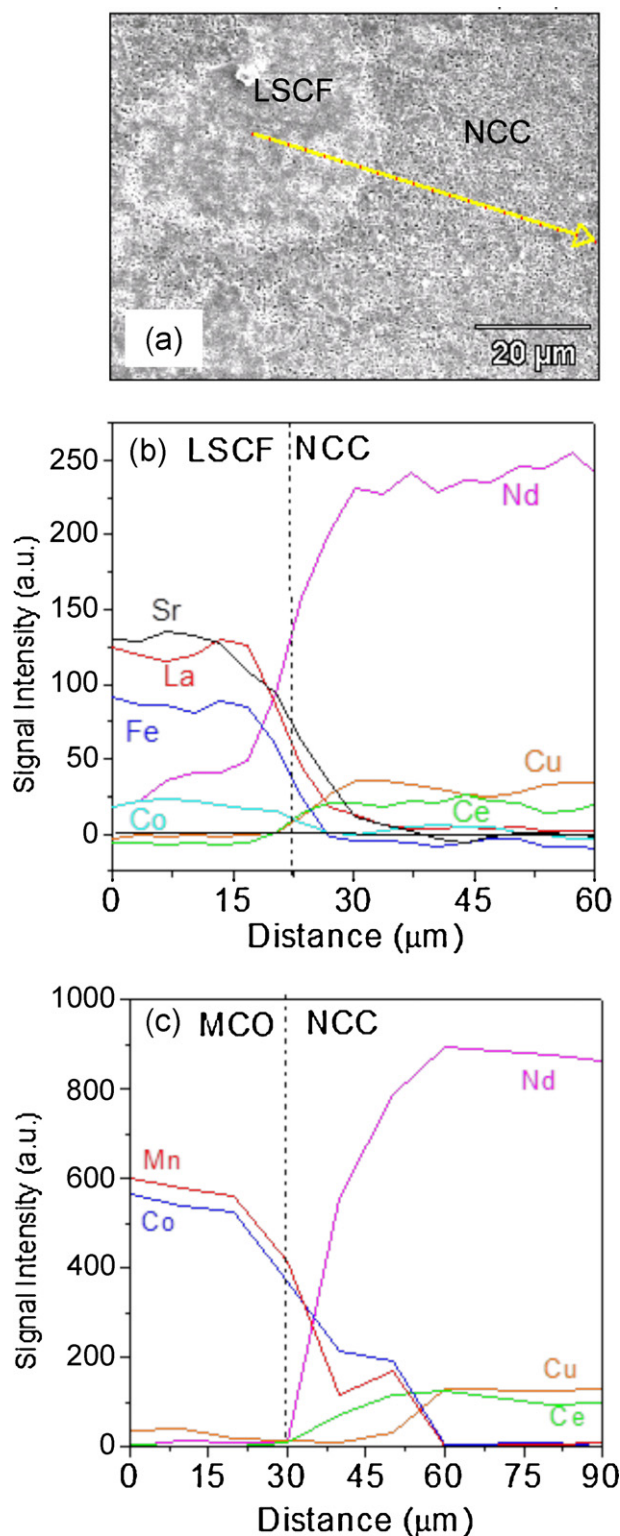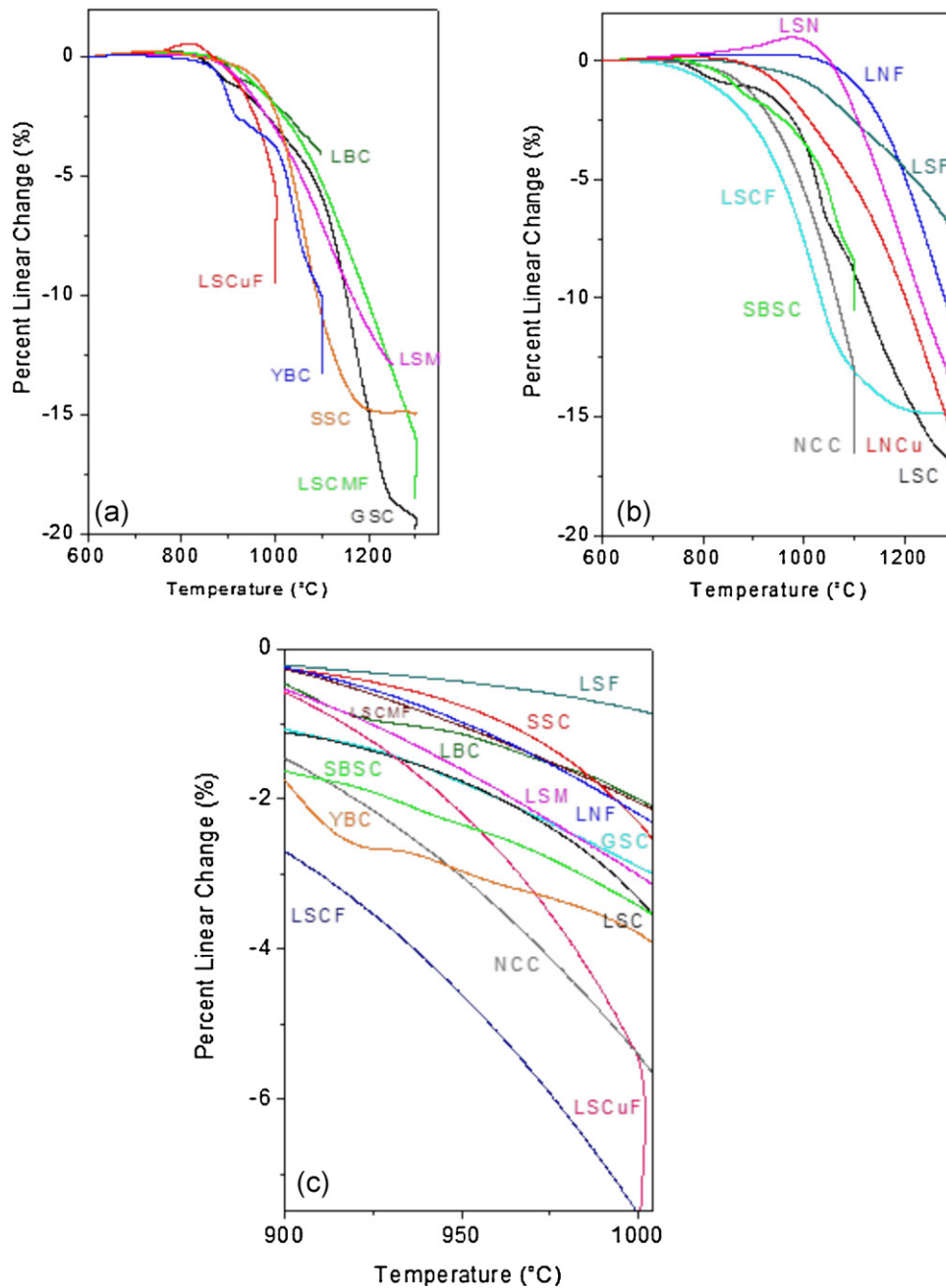
Fig. 10. Sintering behavior for various CCM candidates as determined by dilatometry. The compositions are shown in two plots (a) and (b) for clarity. (c) Shrinkage in the range 900–1000 °C, of relevance to CCM bonding.

4.5. Sintering behavior

Setting a CCM bonding temperature of 900–1000 °C means that minimal sintering is expected. To ensure the best bonding and electrical contact possible, it is desirable to select a composition which sinters significantly at this low temperature. Sintering curves for each composition were determined by dilatometry in air. Fig. 10a, and b shows the complete data sets from 600 to 1300 °C. Note that sintering was not complete upon initial heating to even 1300 °C for several compositions, including LSF, LNF, LBC, and LSCMF. Fig. 10c shows the data range relevant to CCM bonding at 900–1000 °C. Almost no sintering is achieved in this range for LSF, LNF, and LSN. In contrast, NCC, LSCF, and LSCuF shrink more than 5% at 1000 °C. Note that LSCuF continues to sinter during a temperature hold at 1000 °C, achieving almost 10% final shrinkage.

For each composition, the incipient sintering point and shrinkage at 900 °C and 1000 °C were determined as shown in Fig. 11. The values are reported in Table 3. Fig. 11 shows the data for GSC sintering in the 600–1050 °C range. The incipient sintering point is taken as the maximum in the sintering curve. It is at this point that thermal expansion, which dominates at lower temperatures, is overtaken by sintering, which dominates at higher temperatures. The percent linear change (PLC) value at this point is used as the baseline for determining shrinkage at 900 °C and 1000 °C.

4.6. Screening summary

Table 3 summarizes the findings of Sections 4.1–4.5. The values for the important screening parameters are reported, and assigned
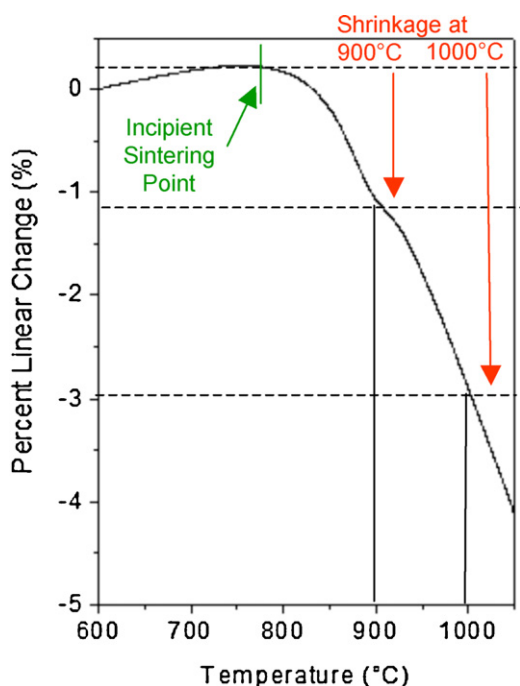
Fig. 11. Sintering behavior for GSC. The markings on the plot show how the incipient sintering point and shrinkage at 900 and 1000 °C are determined.

a color indicating the relative merit of each candidate for each parameter. Some broad observations can be drawn from Table 3:

- Very few compositions achieved significant sintering at 900 °C, but many shrank more than 3% at 1000 °C. This suggests that using the highest CCM bonding temperature possible (constrained by oxidation of the interconnect) can greatly broaden the choice of candidates that are expected to produce a strong CCM layer.
- The cobalt-containing compositions displayed the highest CTEs observed. These included all of the layered perovskite ($ABCo_2O_{5+\delta}$) structures studied.
- The great majority of candidates did not react significantly with MCO. This is a desirable result, as interconnects typically have only a thin layer of MCO coating. In contrast, most did react with LSCF. This may be acceptable, however, if the LSCF cathode layer is thick enough that the reaction zone does not reach the buried electrochemically active region near the cathode/electrolyte interface.
- Only LSC and SSC stand out as providing much higher conductivity than the other candidates.

Based on this screening summary, we down-selected to a few most promising candidates, which were then subjected to long-term ASR testing as described below in Section 4.7. Unfortunately, no single composition provided both high conductivity and high sintering at 1000 °C. LSCF and LSCuF were chosen on the basis of very good sintering, and moderate conductivity. LSC and SSC were chosen on the basis of excellent conductivity and moderate sintering. We also chose NCC, because it was the only candidate that reacted with both MCO and LSCF and it is possible that reaction at the CCM/MCO and CCM/cathode interfaces may improve bonding.

4.7. ASR measurements

ASR measurements were performed using the "half-assembly" geometries shown in Fig. 2. The intention in employing these geometries is to independently observe the ASR of the CCM/LSCF and CCM/MCO-441 interfaces relevant to an operating fuel cell
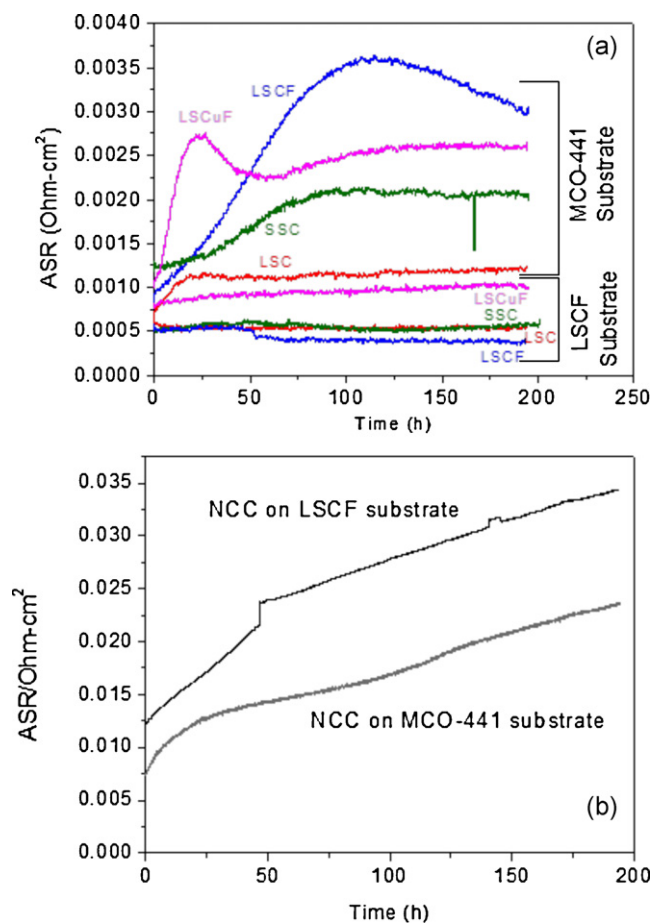

Fig. 12. ASR of various half-assemblies at 800 °C in air. (a) CCM/LSCF and (b) CCM/MCO-441 assemblies. (c) ASR of NCC/LSCF (black) and NCC/MCO-441 (gray).

stack. This work provides a baseline for future work involving in situ tests with operating fuel cells.

The results for CCM/LSCF half-assembly ASR testing are shown at the bottom of Fig. 12a. The specimen marked LSCF is a porous LSCF layer on dense LSCF substrate, thus providing a baseline for the CCM/LSCF specimens. The relative initial ASRs for each candidate CCM follow the trend of the conductivities reported in Table 3. Note that this is not necessarily expected, because the conductivities in Table 3 were measured for dense bars, whereas the conductivity of the porous CCM layer on LSCF substrate will be affected by the bulk conductivity, layer porosity, extent of sintering in the layer, and extent of bonding to the porous LSCF substrate. Although LSC and SSC are not expected to be very well sintered after firing the CCM/LSCF sample at only 1000 °C, their very high bulk conductivity nonetheless result in the lowest initial ASRs of the candidates. The stability of the ASR is quite good for LSCF, LSC, and SSC. The ASR for LSCuF, however, steadily increases over the testing time. We speculate this is due to mobility of Cu.

The results for CCM/MCO-441 half-assembly ASR testing are shown in the top of Fig. 12a. The initial ASR is significantly higher than for the CCM/LSCF samples, consistent with the ASR being dominated by the relatively low-conductivity MCO and Cr_2O_3 layers. The conductivity of MCO is reported to be 66 S cm^{-1} at 800 °C in air, [6,7] and that of Cr_2O_3 ranges from 0.004 to 0.05 S cm^{-1} [24]. LSC provides the lowest, and most stable ASR in this group. The others show rapid increase in ASR over the first 50–100 h, followed by more stable behavior. We surmise this is due to rapid initial chromia scale growth.
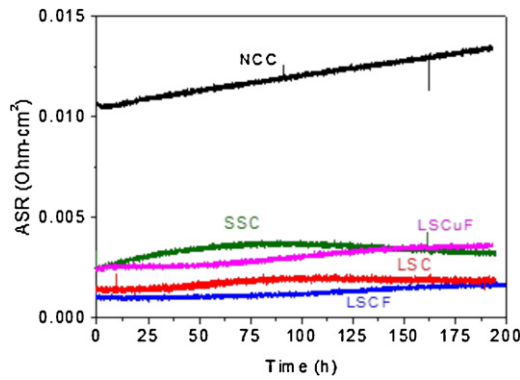
Fig. 13. ASR of various LSCF/CCM/MCO-441 assemblies at 800 °C in air.

For both half-assembly types, NCC shows a very high initial ASR, which degrades rapidly with time (Fig. 12b). Note that initial values are an order of magnitude higher than for the specimens shown in Fig. 12a. Therefore, NCC is eliminated from further consideration as a candidate CCM.

Fig. 13 shows the ASR for LSCF/CCM/MCO-441 assemblies. The ASR values (0.001–0.004 Ω cm^2) are similar to those for the CCM/MCO-441 half-assemblies. This is again consistent with the total ASR being dominated by the MCO and Cr_2O_3 layers.

These observations suggest a few guidelines for selection of the CCM. The CCM should not react deleteriously with LSCF or MCO, as illustrated by the high and unstable ASR of the specimens that incorporated NCC. The CCM should have a high enough conductivity that the total ASR is dominated by MCO and Cr_2O_3. This is a relatively easy requirement to fulfill, and well-sintered materials with relatively low bulk conductivity (such as LSCF or LSCuF) or less-well-sintered materials with high bulk conductivity (such as LSC or SSC) are suitable. Therefore, considerations other than the ASR will be critical in selecting the best CCM. The specimen geometries in this work were chosen to provide relatively low stress on the CCM and its interfaces with LSCF and MCO. In contrast, the CCM is expected to experience much greater mechanical stresses in an operating SOFC stack. Mechanical testing is therefore needed to select between the multiple CCM candidates that provide acceptable electrical properties, and this will be the subject of future work.

4.8. Post-test analysis

After ASR testing, all specimens were cross-sectioned and examined with SEM and EDS. Fig. 14 shows an image of the SSC/MCO-441 half-assembly. Images for all other specimens were qualitatively
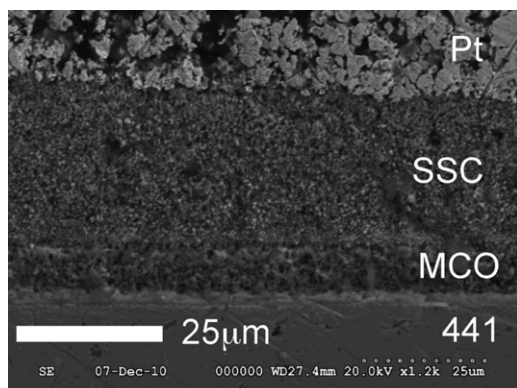

Fig. 14. Cross-sectional SEM image of SSC/MCO-441 half-assembly after ASR testing.
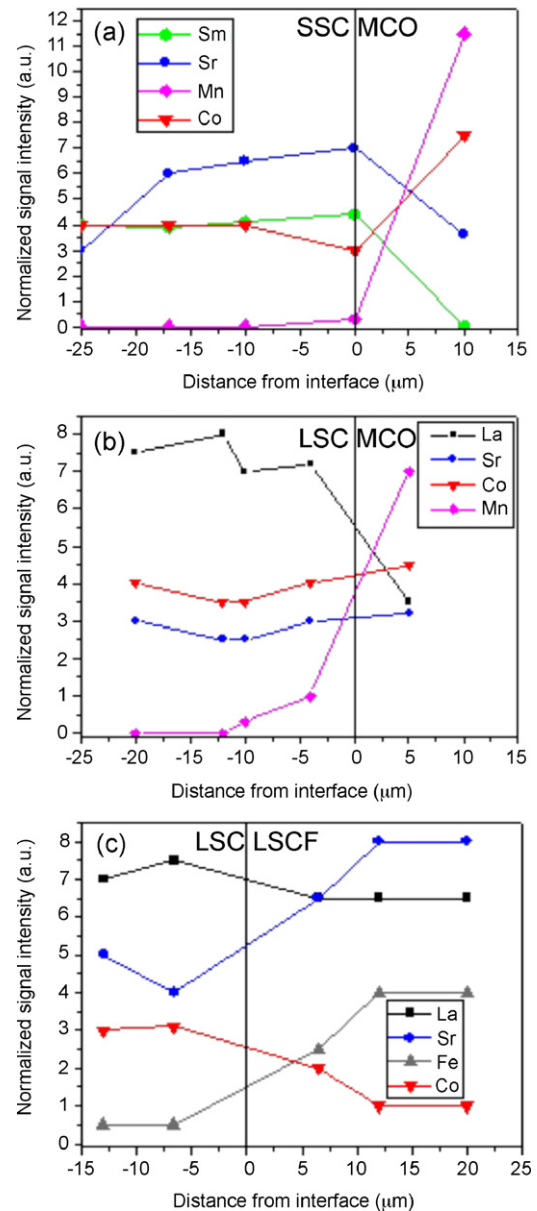

Fig. 15. Post-mortem EDS analysis of interdiffusion at the (a) SSC/MCO, (b) LSC/MCO, and (c) LSC/LSCF interfaces on half-assembly specimens after ASR testing.

similar, and therefore not shown. It is clear in the image that all of the layers are well-bonded to each other, and have sharp interfaces. The microstructure of the SSC and MCO layers are relatively homogeneous, and in particular no cracks or large voids are observed.

EDS was used to estimate the extent of interdiffusion of CCM and MCO or CCM and LSCF across their interfaces. Linescans were produced from a series of small area scans on a transect of the CCM/MCO or CCM/LSCF interface. Representative results are shown in Fig. 15 and the complete set of qualitative observations is presented in Table 4. Further work would be necessary to quantify the degree and distance of interdiffusion, but these qualitative observations give some important insight. In all cases, significant reaction between the materials is not observed. Some interdiffusion is observed, but it is generally limited to the area near the interface. In particular, Sr enrichment of the MCO layer is observed for both LSC and SSC. This is not surprising, as Sr is known to be mobile in the cathode environment [25–27]. Because the extent of interdiffusion into LSCF is minimal, and limited to the region of the CCM/LSCF interface, we do not expect significant impact on

Table 4
Qualitative assessment of interdiffusion of foreign elements observed with EDS for CCM/LSCF and CCM/MCO interfaces.

	CCM	LSCF	CCM	MCO
Minor	Fe	None	Minor Mn	La, Sr
SSC	Minor Fe	Minor Sm	None	Sr
LSCF	N/A	N/A	None	Fe
LSCuF	None	Minor Cu	None	Minor Fe/Cu
NCC	None	None	Minor Mn	Minor Nd/Cu/Ce

the cathode performance in an operating cell; the electrochemically active LSCF/electrolyte interface is well removed from the LSC/CCM interface. In contrast, the MCO layer is relatively thin and diffusion of elements from the CCM (or leaching of Mn or Co from MCO into the CCM) can affect a significant portion of the MCO layer. We suspect therefore that the electrical conductivity and oxygen permeability of the MCO layer may depend on the identity of the CCM. Thus, the chromia growth rate, and long-term performance of the MCO layer likely depends on the CCM composition. Future work will explore this relationship in more detail.

5. Conclusions

A list of candidate CCM compositions was identified from the SOFC cathode literature. The candidates were screened for conductivity, sintering behavior, CTE, and tendency to react with MCO or LSCF. The most promising candidates suggested by this screening were LSCF, LSCuF, SSC and LSC. These were tested for ASR on LSCF and MCO-coated 441 coupons. The ASR observed for CCM/MCO-441 specimens was larger and displayed lower initial stability than for CCM/LSCF specimens. We therefore conclude that the ASR in the LSCF/CCM/MCO-441 stack is dominated by MCO and Cr_2O_3. On both substrates, LSC and SSC provided the lowest and most stable ASR, although LSCF and LSCuF are also acceptable. Electrical properties are acceptable after sintering to $1000\,°C$. Further selection between these materials will depend on mechanical integrity of the CCM/LSCF and CCM/MCO interfaces. Future work will include mechanical testing of the CCM/LSCF and CCM/MCO-441 interface adhesion, and in situ operation of full cells with various CCM compositions.

Acknowledgements

References

[1] Z. Yang, G. Xia, P. Singh, J.W. Stevenson, J. Power Sources 155 (2006) 246–252.
[2] X. Montero, F. Tietz, D. Stover, M. Cassir, I. Villarreal, J. Power Sources 188 (2009) 148–155.
[3] S. Simner, M. Anderson, J. Bonnett, J. Stevenson, Solid State Ionics 175 (2004) 79–81.
[4] B.P. McCarthy, L.R. Pederson, Y.S. Chou, X.-D. Zhou, W.A. Surdoval, L.C. Wilson, J. Power Sources 180 (2008) 294–300.
[5] J.W. Fergus, Mater. Sci. Eng. A 397 (2005) 271–283.
[6] Z. Yang, G. Xia, G.D. Maupin, J.W. Stevenson, Surf. Coat. Technol. 201 (2006) 4476–4483.
[7] Z. Yang, G. Xia, X.-H. Li, J.W. Stevenson, Int. J. Hydrogen Energy 32 (2007) 3648–3654.
[8] M. Cassidy, J.T.S. Irvine, ECS Trans. 25 (2) (2009) 2689–2698.
[9] X. Montero, F. Tietz, D. Stover, M. Cassir, I. Villareal, J. Power Sources 188 (2009) 148–155.
[10] X.W. Song, C.Y. Zhong, F. Zhou, X.H. Hao, G.X. Jia, S.L. An, ECS Trans. 25 (2) (2009) 2607–2616.
[11] J.H. Kim, J. Bae, M. Cassidy, P.A. Connor, W. Zhou, J.T.S. Irvine, ECS Trans. 25 (2) (2009) 2707–2715.
[12] X. Zhang, H. Hao, X. Hua, Physica B 403 (2008) 3406–3409.
[13] T. Inprasit, P. Limthongkul, S. Wongkasemjit, ECS Trans. 25 (2) (2009) 2581–2588.
[14] C. Xia, W. Rauch, F. Chen, M. Liu, Solid State Ionics 149 (2002) 11–19.
[15] K. Swierczek, M. Gozu, J. Power Sources 173 (2007) 695–699.
[16] E. Konysheva, J.T.S. Irvine, J. Power Sources 193 (2009) 175–179.
[17] J.-H. Kim, F. Prado, A. Manthiram, J. Electrochem. Soc. 155 (2008) B1023–B1028.
[18] J.-H. Kim, A. Manthiram, J. Electrochem. Soc. 155 (2008) B385–B390.
[19] A. Aguadero, J.A. Alonso, M.J. Escudero, L. Daz, Solid State Ionics 179 (2008) 393–400.
[20] S. Yang, T. He, Qiang He, J. Alloys Compd. 450 (2008) 400–404.
[21] M. Bevilacqua, T. Montini, C. Tavagnacco, G. Vicario, P. Fornasiero, M. Graziani, Solid State Ionics 177 (2006) 2957–2965.
[22] S. Megel, K. Eichler, N. Trofimenko, S. Hoehn, Solid State Ionics 177 (2006) 2099–2102.
[23] S. Wang, M. Katsuki, M. Dokiya, T. Hashimoto, Solid State Ionics 159 (2003) 71–78.
[24] P. Huczkowski, N. Christiansen, V. Shemet, L. Niewolak, J. Piron-Abellan, L. Singheiser, W.J. Quadakkers, Fuel Cells 06 (2006) 93–99.
[25] G.Y. Lau, M.C. Tucker, C.P. Jacobson, S.J. Visco, S.H. Gleixner, L.C. DeJonghe, J. Power Sources 195 (2010) 7540–7547.
[26] C. Sun, R. Hui, J. Roller, J. Solid State Electrochem. (2010) 1125–1144.
[27] S. Taniguchi, M. Kadowaki, H. Kawamura, T. Yasuo, Y. Akiyama, Y. Miyake, T. Saitoh, J. Power Sources 55 (1995) 73–79.